

Quantum Solvation of Carbonyl Sulfide with Helium Atoms

Jian Tang,¹ Yunjie Xu,² A. R. W. McKellar,^{1*} Wolfgang Jäger^{2*}

High-resolution infrared and microwave spectra of He_N-carbonyl sulfide (He_N-OCS) clusters with *N* ranging from 2 to 8 have been detected and unambiguously assigned. The spectra show the formation of a solvation layer beginning with an equatorial "donut" of five helium atoms around the OCS molecule. The cluster moment of inertia increases as a function of *N* and overshoots the liquid droplet limit for *N* > 5, implying that even atoms in the first solvation shell are decoupled from the OCS rotation in helium nanodroplets. To the extent that this is due to superfluidity, the results directly explore the microscopic evolution of a phenomenon that is formally macroscopic in nature.

rests on the difficulty of recreating the microstructure of macroscopic objects down to atomic length scales. This approach replaces the number-theoretical conjectures of current cryptosystems with technological constraints that have no theoretical grounding, but that do present daunting practical challenges to adversaries. Such practical limits are perhaps the most important point of all: Cryptosystems don't protect information if they're not used. The introduction of physical one-way functions greatly expands where, and how, information can be protected.

References and Notes

1. R. L. Rivest, A. Shamir, L. Adleman, *Commun. ACM* **21**, 120 (1978).
2. W. Diffie, M. Hellman, *IEEE Trans. Inf. Theory* **IT-22**, 644 (1976).
3. M. V. Wilkes, *Time-Sharing Computer Systems* (American Elsevier, New York, 1972).
4. R. Rivest, RFC 1321: The MD5 message-digest algorithm (1992).
5. D. Atkins, M. Graff, A. K. Lenstra, P. C. Leyland, *Advances in Cryptology—ASIACRYPT'94*, J. Pieprzyk, R. N. Safavi, Eds. (Springer-Verlag, Berlin, 1995), pp. 263–277.
6. R. Anderson, M. Kuhn, *Security Protocols, 5th International Workshop*, B. Christianson, B. Crispo, M. Lomas, M. Roe, Eds. (Springer-Verlag, Berlin, 1998), pp. 125–136.
7. P. W. Shor, *SIAM J. Comput.* **26**, 1484 (1997).
8. J. R. Smith, A. V. Sutherland, *Proceedings of AutoID'99, the Workshop on Automatic Identification Advanced Technologies* (IEEE, New York, 1999), pp. 79–83.
9. R. van Renesse, *European Convention on Security and Detection* (Institution of Electrical Engineers London, 1995), pp. 45–49.
10. N. Amer, D. DiVincenzo, N. Gershenfeld, U.S. Patent 5,790,025 (1998).
11. W. K. Wootters, W. Zurek, *Nature* **299**, 982 (1982).
12. J. W. Goodman, *Laser Speckle and Related Phenomena*, J. C. Dainty, Ed. (Springer-Verlag, Berlin, 1975), pp. 9–75.
13. S. Feng, C. Kane, P. A. Lee, A. D. Stone, *Phys. Rev. Lett.* **61**, 834 (1988).
14. S. Feng, P. A. Lee, *Science* **251**, 633 (1991).
15. R. Berkovits, *Phys. Rev. B* **43**, 8638 (1991).
16. R. Pappu, thesis, Massachusetts Institute of Technology, Cambridge, MA (2001).
17. M. C. W. van Rossum, T. M. Nieuwenhuizen, *Rev. Mod. Phys.* **71**, 313 (1999).
18. A. Slocum, *Precis. Eng.* **14**, 67 (1992).
19. O. Nestares, R. Navarro, J. Portilla, A. Taberner, *J. Electron. Imaging* **7**, 166 (1998).
20. D. Gabor, *J. Inst. Electr. Eng.* **93**, 429 (1946).
21. J. G. Daugman, *J. Opt. Soc. Am.* **2**, 1160 (1985).
22. H. V. Poor, *An Introduction to Signal Detection and Estimation* (Springer-Verlag, New York, 1994).
23. B. A. Ridley et al., *Nanophase and Nanocomposite Materials III* (Materials Research Society, Warrendale, PA, 2000), pp. 115–120.
24. J. H. Smith et al., *Proc. SPIE* **3514**, 42 (1998).
25. K. M. Johnson, L. Hesselink, J. W. Goodman, *Appl. Opt.* **23**, 218 (1984).
26. B. van Tiggelen, thesis, University of Amsterdam, Netherlands (1992).
27. A. G. Hoekstra, M. D. Grimminck, P. M. A. Sloom, *Int. J. Mod. Phys. C* **9**, 87 (1998).
28. B. Spivak, A. Zyuzin, *Phys. Rev. Lett.* **84**, 1970 (2000).
29. C. Marxer, N. E. de Rooij, *Sens. Mater.* **10**, 351 (1998).
30. D. Hoadley, P. McConville, O. Norman, N. O. Birge, *Phys. Rev. B* **60**, 5617 (1999).
31. Supported by the Center for Bits and Atoms (NSF grant CCR-0122419) at the MIT Media Labs and an IBM Research Fellowship (R.P.). For many helpful discussions, we thank N. Amer, I. Chuang, D. DiVincenzo, J. Jacobson, W. Plesniak, R. Rivest, D. Simon, J. Smith, and members of the Physics and Media Group. We are especially grateful to A. Juels for several insightful comments and constructive criticism.

28 May 2002; accepted 7 August 2002

One of the fundamental goals of cluster research is the interpretation of the properties of condensed phases in terms of those of their constituent atoms and molecules (1). However, the clusters that can be investigated systematically in detail are limited in size. In the area of superfluidity, the recent development of He nanodroplet isolation spectroscopy (2) helps to close the gap between cluster and bulk studies. It offers possibilities for synthesizing, stabilizing, and characterizing novel chemical species (3) and also constitutes an important step toward detailed microscopic understanding of superfluidity, a collective bulk property.

In an elegant nanomatrix study, the microscopic Andronikashvili experiment, Toennies and co-workers (4) used the appearance of sharp infrared (IR) spectral features of dopant molecules in He nanodroplets (consisting of several thousand He atoms) as an indicator of the onset of the superfluidity. Carbonyl sulfide (OCS) was used as the dopant molecule in ³He droplets in these experiments. Line widths in the OCS spectrum were monitored as a function of the number of captured ⁴He atoms. About 60 ⁴He atoms, corresponding to roughly two solvation layers of ⁴He around OCS, were required to induce sharp gas-phase-like spectral features indicative of nearly free rotation of the molecule. Various models have been advanced to explain the observation (5–7). Explicit simulations (8) show that the decoupling of the solvent from the molecule is associated with the onset of superfluidity (5).

Can the onset of superfluidity be fully traced using high-resolution spectroscopy in the small to intermediate cluster size regime, and which observables can be used as indicators of superfluidity? Advances in theoret-

ical models and computing power may give answers to the latter question. Simulations provide predictions of observable properties such as frequency shifts and rotational constants, along with nonobservables, such as He density profiles and superfluid character. Gianturco, Whaley, and co-workers (5, 9, 10) performed diffusion Monte Carlo calculations for He_N-OCS clusters with *N* = 1 to 100 and found a sharp energy signature upon completion of the first solvation shell at *N* ≈ 20. The CO vibrational frequency saturated at *N* ≈ 20 and reached a value in qualitative agreement with nanodroplet experiments (4). Simulations also suggest that the rotational constant *B* (proportional to the inverse moment of inertia) of He_N-molecule systems saturates at relatively small *N*; for example, *N* = 8 for the SF₆ molecule (5), attaining the limiting nanodroplet value (11).

An ideal experiment would isolate small-to medium-sized He_N-molecule clusters and characterize them sequentially until dramatic changes in spectroscopic observables indicated the onset of superfluidity. He_N-OCS is an ideal test system because OCS is a strong chromophore in both the IR and the microwave regions. In addition, the He_N-OCS complex is well characterized spectroscopically (12, 13) and several high-quality potential energy surfaces (PESs) have been constructed for it (12, 14, 15).

We have measured and assigned rotationally resolved microwave and IR spectra of He_N-OCS clusters with *N* = 2 to 8 and observed IR spectra of larger clusters with *N* up to about 20. The experiments were carried out using an IR diode laser spectrometer and a molecular beam Fourier-transform microwave spectrometer, as described previously (16–18). Clusters were generated using pulsed supersonic jet expansions of trace amounts (<0.1%) of OCS in He at backing pressures ranging from 10 to 30 atm. For the larger clusters, the jet nozzles were cooled to temperatures as low as –80°C. Microwave spectra of the singly substituted minor isotopomers were observed in natural abundance,

¹Stacie Institute for Molecular Sciences, National Research Council of Canada, Ottawa, Ontario K1A 0R6, Canada. ²Department of Chemistry, University of Alberta, Edmonton, Alberta T6G 2G2, Canada.

*To whom correspondence should be addressed. E-mail: robert.mckellar@nrc.ca (A.R.W.M.); wolfgang.jaeger@ualberta.ca (W.J.)

20 September 2002

Science

Vol. 297 No. 5589
Pages 1945-2156 \$9



AMERICAN ASSOCIATION FOR THE ADVANCEMENT OF SCIENCE

REPORTS

whereas those of doubly substituted isotopomers of OCS were measured using an enriched sample (99% ^{13}C and 12% ^{18}O). The yield of specific clusters could be partly controlled by adjusting the sample temperature, pressure, and composition. Unambiguous assignments were ultimately achieved by combining the advantages of IR and microwave spectroscopy. The broadband nature of the IR spectra made it possible to recognize band structures and vibrational shifts, whereas the high resolution and sensitivity of the microwave spectra allowed detection of minor isotopomers and resolution of narrow hyperfine splittings, which were critical for the final spectral assignments. Much lower-resolution vibronic spectra of He clusters in a similar size range have been reported (19).

Part of the IR spectrum of $\text{He}_N\text{-OCS}$ clusters observed in the region of the C-O stretching vibration of OCS ($\approx 2062\text{ cm}^{-1}$) with different backing pressures is shown in Fig. 1. A key result is the shift of the $\text{He}_N\text{-OCS}$ cluster band origins with respect to that of the free OCS molecule (20). This vibrational shift is plotted in Fig. 2 as a function of cluster size. For $N = 1$ to 5, the experimental band origins show a

positive blue frequency shift with an almost constant increment, which indicates that the first five He atoms occupy positions equivalent to that found in He-OCS (12, 13). This structure forms a He “donut” around the equator of the OCS molecule until space saturation is reached. With the addition of the sixth, seventh, and eighth He atoms, the shift turns negative and leads toward its ultimate limiting value for He nanodroplets (4). The dependence of the band shift on the position of the He atoms demonstrates the delicate influence of intermolecular interactions on the ground- and excited-state PESs. Also shown in Fig. 2 in red are results of a recent theoretical prediction (9). This calculation reproduces the overall red shift seen in nanodroplets qualitatively but fails to account for the observed blue shift in the range $N = 1$ to 5 and the subsequent turnaround toward the red. This may be the result of an inadequate PES used or of approximations in the calculations.

The dependence of the spectra on sample pressure and temperature, together with the regularity of the vibrational shifts (especially for $N = 1$ to 5), provided the foundation for assigning N in the IR spectra. The low rotational temperatures ($<1\text{ K}$) in the jet expansion al-

lowed us to follow the IR bands only up to low rotational quantum numbers, $J = 3$ or 4, and it was therefore important to validate the N and J assignments using microwave transitions. Microwave detection of minor isotopomers can also provide information about the positions of the “solvating” He atoms.

Microwave searches were carried out simultaneously for several isotopomers of the same cluster. Corresponding transitions of different isotopomers were tested for consistent behavior with sample pressure and nozzle temperature. The observation of nuclear quadrupolar hyperfine structure for isotopomers containing ^{33}S or ^{17}O (nuclear spin $I = 3/2$ and $5/2$, respectively) helped to make the assignments unique. Links between successive rotational transitions of the same isotopomer were verified using microwave-microwave double resonance (21) to confirm the presence of a common energy level. In all, rotational transitions of five to seven different isotopomers were measured for each $\text{He}_N\text{-OCS}$ ($N = 2$ to 8) cluster, with J ranging from 0 to 4.

For the main isotopomers, $\text{He}_N\text{-}^{16}\text{O}^{12}\text{C}^{32}\text{S}$ ($N = 2$ to 8), the combined IR and microwave data were used to derive spectroscopic parameters (Table 1). For $N = 2$, the spectra are those of an asymmetric top molecule, so A , B , and C rotational constants and centrifugal distortion constants (22) were fitted to $K = 0$ transitions. Ultimately, a more detailed analysis should be possible (23). For $N = 3$ to 5, the spectra could be analyzed as $K = 0$ transitions using a symmetric top model with rotational parameter B and distortion parameters D_J and H_J . For $N = 6$ to 8, we also used a symmetric top model, but it was necessary to vary as many parameters as observed transitions to obtain a good fit. The need for this latter step may be indicative of very nonrigid behavior or slightly asymmetric top structure.

Fig. 1. Part of the observed IR spectrum of $\text{He}_N\text{-OCS}$ clusters. The traces are stacked as a function of backing pressure, from lower pressures at the bottom to higher pressures at the top. Increasing pressure gives larger clusters. Some transitions are labeled with N , the number of He atoms in the cluster (black labels for $J = 0 \leftarrow 1$ transitions, red labels for $J = 1 \leftarrow 0$ transitions, and blue labels for $J = 2 \leftarrow 1$ transitions). Stronger unlabeled features are all due to known OCS and He-OCS transitions, whereas some weaker unlabeled features between 2062.2 and 2062.6 cm^{-1} are due to transitions of clusters with $N > 8$ (not yet assigned in detail).

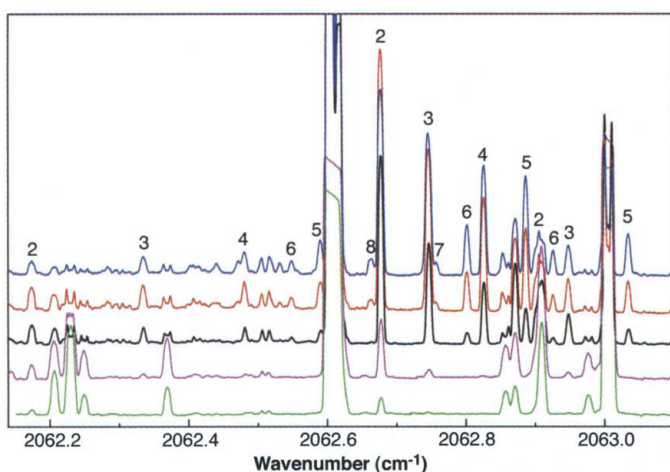


Table 1. Experimental vibrational frequencies and rotational parameters for $^4\text{He}_N\text{-}^{16}\text{O}^{12}\text{C}^{32}\text{S}$ clusters. For $N = 1$ and 2, which are asymmetric rotors, B refers to $(B + C)/2$. The least significant digits given indicate the uncertainties of the parameters.

Species	Vibrational frequency (cm^{-1})	B (MHz)	D_J (MHz)
OCS (20)	2062.2008	6081.5	0.001
He-OCS (12, 13)	2062.3125	4582.8	0.94
He ₂ -OCS	2062.4263	3782.8	5
He ₃ -OCS	2062.5413	3104.6	5.11
He ₄ -OCS	2062.6539	2591.9	0.881
He ₅ -OCS	2062.7401	2225.2	0.234
He ₆ -OCS	2062.6753	1910.5	2.60
He ₇ -OCS	2062.6327	1683.0	1.29
He ₈ -OCS	2062.5676	1447.7	2.00
He nanodroplet-OCS (4)	2061.644	2194.5	11.4

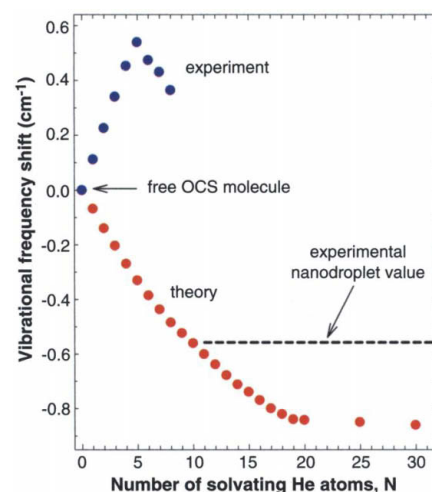


Fig. 2. Observed (blue circles, present work) and calculated [red circles (9)] vibrational frequency shifts for $\text{He}_N\text{-OCS}$ clusters with N in the range from 0 to 30. The dashed horizontal line indicates the observed value for He nanodroplets where $N \approx 10^4$ (4).

The experimental rotational constants B are plotted in Fig. 3 as a function of cluster size, N . The dashed horizontal line indicates the limiting value for larger He nanodroplets (4). Simulations of $\text{He}_N\text{-SF}_6$ clusters (5, 24) indicated that the B values drop with increasing N and reach saturation at $N \approx 8$ at a value near to the nanodroplet value [see figure 2 of (5)]. Theoretical treatments of $\text{He}_N\text{-OCS}$ (5, 10) indicate similar behavior [see figure 16 of (5) and figure 3 of (10)] and suggest saturation of the rotational constant at small N values. This prediction is surprising because one does not expect the system to be superfluid in this regime. Rather, one expects moments of inertia to continue to increase (and rotational constants to decrease) as more He atoms are added. The experimental trend shown in Fig. 3 is in agreement with intuition, and the experimental values undershoot the nanodroplet value; i.e., the value in the limit of superfluidity. From Fig. 3, it is apparent that the rotational constants must increase at a yet to be determined critical N value with the addition of further He atoms. Such an increase in B , corresponding to a decrease in the moment of inertia, cannot be due to structural reorganization, because positions near the inertial axis are already occupied. Rather, the additional He atoms will cause some of the existing He atoms to decouple from the rotational motion of the OCS subunit and decrease the contribution of the first solvation shell to the moment of inertia. In terms of a superfluid model for molecular rotation in the He nanodroplets,

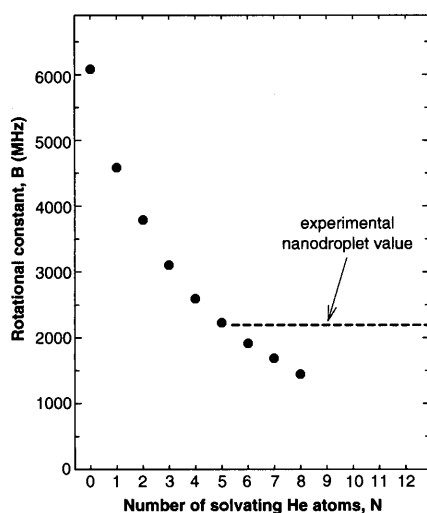


Fig. 3. Observed rotational constants B for $\text{He}_N\text{-OCS}$ clusters with N in the range from 0 to 8. These are proportional to the inverse of the moment of inertia. The horizontal dashed line indicates the observed value for He nanodroplets ($N \approx 10^4$) (4). This is close to our value for $N = 5$, and the clusters with $N = 6, 7$, and 8 actually have smaller B values (larger rotational moments of inertia) than does OCS in He nanodroplets.

this corresponds to participation of He atoms (density) from the first solvation shell in the superfluid He fraction. A theoretical description of the turnaround of the rotational constants has yet to be developed. Such a model will shed further light on the concept of superfluidity in this size regime.

The B rotational constant of $\text{He}_5\text{-OCS}$, where the most favorable positions for the He atoms are fully occupied, is very close to the nanodroplet B value. This result had been predicted in terms of the donut model (25), where the nanodroplet B value was interpreted in terms of five or six He atoms rigidly attached to the OCS molecule. However, the experimental value of the centrifugal distortion constant D_J for $\text{He}_5\text{-OCS}$ is several orders of magnitude smaller than the nanodroplet value. In fact, D_J for $\text{He}_5\text{-OCS}$ is the smallest of all of the clusters reported here, an indication that it is the cluster with the greatest rigidity and stability. This idea is supported by the observed intensities in the spectra, where $\text{He}_5\text{-OCS}$ transitions tended to be stronger than expected relative to those for $N = 4$ and 6. The large nanodroplet value for D_J is therefore probably a further consequence of a significant decoupling of He atoms in the first solvation layer from the OCS rotation.

Analysis of the rotational constants of the $\text{He}_N\text{-OCS}$ clusters gave qualitative structural information. A proposed geometry for the $\text{He}_8\text{-OCS}$ cluster, based on the isotopic data, is shown in Fig. 4. The equivalent donut positions of the first five He atoms are confirmed by the relatively constant moment of inertia increment of the normal isotopomers [about 32.1 atomic mass units \AA^2 (u \AA^2)] in $\text{He}_N\text{-OCS}$ for $N = 3$ to 4 and 4 to 5. Larger moment of inertia increments occur for $N = 5$ to 6, 6 to 7, and 7 to 8 (37.4, 35.7, and 48.8

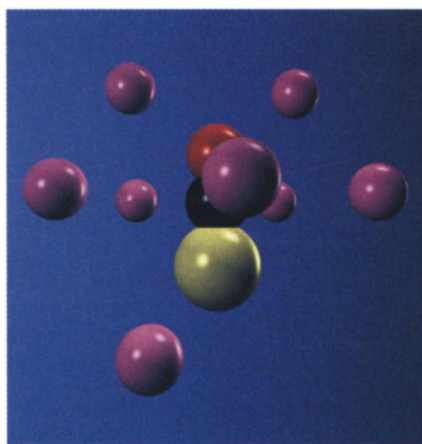


Fig. 4. A proposed structure for the $\text{He}_8\text{-OCS}$ cluster, which is consistent with the isotopic shifts in our observed microwave spectra. The He donut ring is visible in a plane perpendicular to the paper plane and the OCS axis. The solid spheres indicate the van der Waals radii of the atoms; the He atoms are not rigidly attached at the indicated positions but are substantially delocalized.

u \AA^2 , respectively), indicating that these atoms occupy positions further away from the b -rotational axis of the cluster. The B constants of multiple isotopomers for the species with $N = 6$ and 7 indicate that He atoms 6 and 7 settle closer to the O end of OCS. The position of He atom 8 at the S end is consistent with the smaller isotopic data set for $N = 8$ but is less certain. He atoms 6 and 7 move to the O end of OCS despite the fact that the deeper secondary potential energy minimum in He-OCS is at the S end (12, 14, 15). This can be rationalized [see also (12)] to be a consequence of a lower zero-point energy level supported by the shallower but broader well at the O end.

Our results illustrate the possibility of using direct high-resolution spectroscopic measurements of small- and medium-sized clusters ($N \approx 3$ to 20) to “fill the gap” between isolated molecules and the He nanodroplet environment. As such, they explore the microscopic basis of solvation effects and should shed new light on the origin of superfluidity. The observation of rotational moments of inertia for $\text{He}_6\text{-OCS}$, $\text{He}_7\text{-OCS}$, and $\text{He}_8\text{-OCS}$ that are distinctly larger than that of OCS in He nanodroplets suggests that even He atoms in the first solvation shell contribute to the superfluid He fraction in the nanodroplets.

References and Notes

1. A. Stace, *Science* **294**, 1292 (2001).
2. C. Callegari, K. K. Lehmann, R. Schmied, G. Scoles, *J. Chem. Phys.* **115**, 10090 (2001).
3. K. Nauta, D. T. Moore, P. L. Stiles, R. E. Miller, *Science* **292**, 5516 (2001).
4. S. Grebenev, J. P. Toennies, A. F. Vilesov, *Science* **279**, 2083 (1998).
5. Y. Kwon, P. Huang, M. V. Patel, D. Blume, K. B. Whaley, *J. Chem. Phys.* **113**, 6469 (2000).
6. V. S. Babichenko, Yu. Kagan, *Phys. Rev. Lett.* **83**, 3458 (1999).
7. C. Callegari *et al.*, *Phys. Rev. Lett.* **83**, 5058 (1999).
8. D. M. Ceperley, *Rev. Mod. Phys.* **67**, 279 (1995).
9. F. Paesani, F. A. Gianturco, K. B. Whaley, *J. Chem. Phys.* **115**, 10225 (2001).
10. ———, *Europhys. Lett.* **56**, 658 (2001).
11. M. Hartmann, R. E. Miller, A. F. Vilesov, J. P. Toennies, *Phys. Rev. Lett.* **75**, 1566 (1995).
12. K. Higgins, W. Klemperer, *J. Chem. Phys.* **110**, 1383 (1999).
13. J. Tang, A. R. W. McKellar, *J. Chem. Phys.* **115**, 3053 (2001).
14. J. M. M. Howson, J. M. Hutson, *J. Chem. Phys.* **115**, 5059 (2001).
15. F. A. Gianturco, F. Paesani, *J. Chem. Phys.* **113**, 3011 (2000).
16. C. Xia, A. R. W. McKellar, Y. Xu, *J. Chem. Phys.* **113**, 525 (2000).
17. Y. Xu, W. Jäger, *J. Chem. Phys.* **106**, 7968 (1997).
18. ———, *Chem. Phys. Lett.* **350**, 417 (2001).
19. U. Even, I. Al-Hroub, J. Jortner, *J. Chem. Phys.* **115**, 2069 (2001).
20. A. G. Maki, J. S. Wells, *Wavenumber Calibration Tables from Heterodyne Frequency Measurements* (National Institute of Standards and Technology Special Publication 821, U.S. Government Printing Office, Washington, DC, 1991).
21. V. N. Markov, Y. Xu, W. Jäger, *Rev. Sci. Instrum.* **69**, 4061 (1998).
22. J. K. G. Watson, in *Vibrational Spectra and Structure: A Series of Advances*, J. R. Durig, Ed. (Elsevier, New York, 1977), vol. 6, pp. 1–89.

23. M. I. Hernandez, N. Halberstadt, W. D. Sands, K. C. Janda, *J. Chem. Phys.* **113**, 7252 (2000).
 24. E. Lee, D. Farrelly, K. B. Whaley, *Phys. Rev. Lett.* **83**, 3812 (1999).
 25. S. Grebenev et al., *J. Chem. Phys.* **112**, 4485 (2000).

26. Supported by the Natural Sciences and Engineering Research Council of Canada and by the National Research Council of Canada. We thank P. N. Roy and J. K. G. Watson for comments on the manuscript, R. Lipiecki for the microwave coupling device, and M. C.

L. Gerry for the loan of a synthesizer. We also thank the anonymous referees for their suggestions that helped to clarify the manuscript.

8 May 2002; accepted 16 August 2002

Autocatalytic Oxidation of Lead Crystallite Surfaces

Konrad Thürmer,¹ Ellen Williams,¹ Janice Reutt-Robey^{2*}

Growth of an ultrathin lead oxide layer causes massive changes in the shape of lead crystallites. The dynamics of this process was investigated with time-lapsed scanning tunneling microscopy. Pure lead crystallites proved extremely resistant to oxidation. Once nucleated by surface impurities, monolayer films of lead oxide grew readily on lead (111) microfacets in an autocatalytic process. The anisotropic growth of orthorhombic lead oxide films (massicot structure) was most rapid along the direction of weakest lead-oxygen bonding, which suggests that the growth edge autocatalyzes oxygen dissociation by providing proximal sites for oxygen dissociation and attachment.

Thin oxide films, formed by direct reaction between metal surfaces and gaseous O₂, are widely used as catalysts, sensors, dielectrics, and corrosion inhibitors. Studies of the kinetics of oxide growth have shown that once a stable oxide layer forms, the rate of oxidation is limited by field-enhanced transport of ionic species across the oxide film [the Mott-Cabrera model (1)]. Oxide growth thus occurs most rapidly for thinner films but then slows dramatically by transport through thicker films, resulting in a parabolic growth law.

Unfortunately, the Mott-Cabrera model omits the initial stage of oxidation, which is crucial for growing uniform ultrathin oxides of current technological interest, and there have been surprisingly few experimental studies of this critical regime. The initial stage is generally assumed to proceed via the formation of a chemisorbed O monolayer, followed by the nucleation, growth, and coalescence of two-dimensional oxide islands. The saturating O monolayer offers a simple, yet often invalid, assumption: Transition metal systems, such as O/Ru(0001) (2) and O/Ag(110) (3), support chemisorption beyond the monolayer via the dissolution of atomic O and the formation of a variety of O species. For example, emergent RuO₂ patches strongly mediate O uptake by increasing the dissociative sticking coefficient of O₂ by up to six orders of magnitude (4, 5) by the adsorption and subsequent dissociation of O₂ on RuO₂ (6). Simple metal surfaces, in contrast, cannot easily dissociate molecular O₂ (7), hindering the accumulation of even

monolayer quantities. We now report the direct imaging and temporal evolution of PbO films in the nanometer-thickness regime at elevated temperatures. Trace surface impurities are needed to form oxide nuclei on a Pb crystallite surface. Once nucleated, PbO grows autocatalytically in two dimensions. The growth anisotropy of individual PbO grains implicates the dissociation of O₂ as the rate-limiting step. The applicability of this mechanism to other materials systems and technologies is discussed.

Pb crystallites were selected as the model system for these investigations because of the extensive knowledge of the pure crystallite shape derived from scanning electron microscopy (8, 9), scanning tunneling microscopy (STM) (10, 11), and first-principles theoretical calculations (12). Defect-free Pb crystallites can be prepared on a Ru(0001) [or graphite or Cu(001)] support with exposed (111) top facets and (111) and (100) side facets. The rounded crystallite edges display a 3/2 power law (13), indicating that the crystal shape is locally equilibrated. Energetic values for both step and kink formation energies have also been evaluated for this system (10). Pb crystallites are inert with respect to all chamber residual gases (H₂, CO, and CO₂), and the effects of O₂ are thus easily isolated.

We prepared ~1- μ m Pb crystallites under ultrahigh vacuum (UHV) conditions by the room-temperature deposition of a 20- to 30-nm Pb film onto a clean Ru(0001) substrate and subsequent dewetting at temperature (T) ~620 K, or 20 K above the Pb melting temperature, T_m (10). The molten Pb droplets were then cooled at a rate of 0.3 K s⁻¹ to solidify the droplets into crystallites with few (and in some cases no) imperfections. The crystallites were then typically held at elevated temperatures (T ~380 K) for a period of 2 days in order to

achieve stable near-equilibrium crystal shapes. We then used variable-temperature (VT) STM to follow the oxidation of these supported Pb crystallites during in situ exposure to oxidizing gases (14). In lower resolution measurements, we resolved the movements of individual crystallographic steps and the correlated development of PbO grains. For atomistic details on the structures of these PbO grains, we subsequently imaged the grains with atomic resolution at room temperature (15).

We briefly review the structural features of these truncated Pb crystallites. The uppermost part of a Pb crystallite (Fig. 1A) is capped with a (111) facet that is atomically smooth and has a characteristic diameter of about one-half that of the crystallite. The "noisiness" of the monatomic steps that descend to join the (111) and (100) side facets is caused by fluctuations in the step positions (16). The relatively small kink formation energy of 40 meV (10) leads to substantial edge-atom motion at the 380 K temperature of measurement.

After prolonged O₂ exposures under UHV conditions [5000 Langmuirs (L) of O₂, or 1 \times 10⁻⁶ torr for 5000 s] at 370 K, Pb crystallites undergo massive structural transformation (Fig. 1B). Although the Pb mass is conserved overall, the crystallites develop sharp edges. The curved facet boundary of the Pb crystallite, in particular, yields to oxide-stabilized orientations (see the comparison in Fig. 1C). On the oxidized surface, steps assume the extremely straight (stiff) structures characteristic of an oxide crystal. Remarkably, this gross transformation is accomplished by an oxide layer that is only ~0.5 nm thick. The crystallite can be remelted to remove the oxide layer and restore the Pb crystallite to its neat rounded shape.

These ultrathin oxide-coated crystallites are the results of the billions of surface chemical events. In order to identify these molecular-level processes, we decreased the O₂ pressure to 1 \times 10⁻⁷ torr and limited the exposures to capture the initial stages of this transformation with time-lapsed STM imaging. We determined that impurities play a key role under practical oxidation conditions.

We first examined the oxidation of ultrapure Pb crystallites. Because of the impracticality of imaging the entire crystallite with high resolution, we identify impurity-free surfaces as (i) those which exhibit no impurities when random patches of the surface are imaged with atomic resolution and (ii) those with freely fluctuating step configurations that are completely undistorted

¹Department of Physics, ²Department of Chemistry and Biochemistry, University of Maryland, College Park, MD 20742, USA.

*To whom correspondence should be addressed. E-mail: rrobey@wam.umd.edu